Flow-induced forces for a group of one large and several small structures in the sheared turbulent flow.

ANNAPEH, H.F. and KURUSHINA, V.

2023

fluids

MDPI

Article

Flow-Induced Forces for a Group of One Large and Several Small Structures in the Sheared Turbulent Flow

Henry Francis Annapeh [1] and Victoria Kurushina [1,2,*]

[1] Laboratory of Vibration and Hydrodynamics Modelling, Industrial University of Tyumen, 38 Volodarskogo Street, Tyumen 625000, Russia; kinghenry939@gmail.com
[2] School of Engineering, Newcastle University, Newcastle upon Tyne NE1 7RU, UK
* Correspondence: v.kurushina@outlook.com

Abstract: Evaluating the hydrodynamic force fluctuations acting on each structure in a group of subsea objects of different cross-section shapes, sizes and relative positions represents a challenge due to the sensitivity of the vortex shedding process, especially for a variety of sheared flows. The present study uses the numerical 2D computational fluid dynamics model to estimate the flow-induced forces on a group of small circular and D-shaped cylinders in the linear and parabolic sheared flow, which are placed in proximity to a larger structure of the squared cross-section. This allows us to evaluate loads, which are affected by the presence of subsea equipment located on the seabed. The average Reynolds number of the considered linear flow profile is 3900, while the parabolic flow profile has the maximum Reynolds number of 3900. The k-ω SST turbulence model is used for simulations. The work demonstrates the effect of the cross-sectional shape of smaller cylinders on hydrodynamic coefficients, explores the effect from the spacing in between the structures and highlights differences between loads in the linearly sheared and parabolic flow. The results obtained show that the presence of the squared cylinder notably influences the mean drag coefficient on the first cylinder, for both circular and D-shaped cylinders. The parabolic sheared flow profile in this series leads to the highest mean drag and the highest amplitudes of the fluctuating drag and lift coefficients.

Keywords: flow over cylinder; flow-induced forces; subsea structures; sheared flow; computational fluid dynamics; drag force; lift force; turbulent flow

Citation: Annapeh, H.F.; Kurushina, V. Flow-Induced Forces for a Group of One Large and Several Small Structures in the Sheared Turbulent Flow. *Fluids* **2023**, *8*, 158. https://doi.org/10.3390/fluids8050158

Academic Editors: Jian Fang and D. Andrew S. Rees

Received: 27 March 2023
Revised: 30 April 2023
Accepted: 3 May 2023
Published: 17 May 2023

1. Introduction

Offshore renewable energy systems, complexes for carbon capture and storage and the oil and gas production industry require a wide range of both rigid and flexible and dynamic and stationary slender elements to be involved in the construction, drilling, operation, repairs and decommissioning procedures. The failures of slender structures (especially at the connection sites), disruptions and delays to the operations within these systems may be due to unaccounted occurrences of vortex shedding, which refers to the increased fluctuations of the fluid forces. The structural reliability can be enhanced by considering the sheared flow conditions at the design stages, which becomes particularly challenging when reaching to a seabed at the large depth of 3000 m.

The fundamental basis for the numerical simulation for the flow over a bluff body is established by early numerical studies, such as [1], and reviews focusing on the vortex dynamics phenomena over a single structure [2] and a pair of structures [3]. In the latter work, the downstream cylinder position is close to be in line with the upstream structure and leads to higher lift force amplitudes. Numerical studies for a single structure in the uniform flow develop the LES methodology [4] and consider the advantages and challenges for 2D and 3D flow simulations [5,6]. The very recent work for two structures in a tandem position and in a uniform flow presents the effect of spacing variations on a group of vibrating structures [7].

Sheared flow conditions for a standalone structure are considered in the early numerical studies for a rotating circular structure [8], a stationary circular structure [9] and a squared cylinder [10]. Studies for a circular stationary structure in a sheared flow are focused on testing the numerical schemes [11] and investigating the separation of the boundary layer [12] and the flow effects observed in the subcritical flow regime [13], at a low Reynolds number [14] and for a range of flow regimes [15].

The line of research on the numerical simulation of the fluid-structure interaction in the uniform flow is continued by the works on three cylinders in tandem [16] and four cylinders in a squared arrangement [17–20], with a detailed consideration of the flow interference, hydrodynamic loads and vibration. The latest research [21–25] is focused on the dynamics of three and four flexible structures in tandem and in side-by-side positions, including experimental, numerical results and the identification of energy harvesting perspectives [23]. More advanced arrangements of circular structures investigated to date include: three objects placed in a triangle, studied in [26]; a set of five risers in a cylindrical arrangement [27]; and the use of up to eight control cylinders around protected circular structures, in order to mitigate vortex-induced loads [28]. A separate branch of studies considers the flow over a structure placed close to a plane boundary [29]. The review of existing studies indicates the overall research gap existing in the knowledge of hydrodynamic loads in sheared currents and, specifically, in the knowledge of effects on the vortex-induced loads when groups of structures with mixed shapes and sizes are subjected to both uniform and sheared flows.

The current work continues the branch of numerical simulation studies performed for a group of three-four structures while placed in a planar sheared flow. Previous research in this direction considers circular structures: two objects of a different size [30] in the uniform flow, a group of three small structures in several arrangements [31] and a group of small structures in a triangular layout in proximity to a larger object [32] in both uniform and sheared flows. A large group of structures of different cross-sections is considered in [33], where the D-shape, previously implemented in [34], is found to have a positive effect on the reduction of fluid loads. The current study investigates smaller structures with two distinct cross-sectional shapes: circular and half-circular. These smaller cylinders are placed in proximity to a larger squared structure, following the results in [31]. The arrangement leads to a superposition of generated vortex streets, and the aim of this investigation is to identify scenarios of reduced hydrodynamic loads for the considered range of cases, which would be a practical choice of the structural layout. Two sheared flow profiles are considered, based on the Reynolds number of 3900, corresponding to the developed turbulent flow regime. The computational fluid dynamics model, based on the experience in [35], is designed for these structural arrangements in order to achieve the goals.

The current paper is arranged as follows. Section 1 outlines the existing research background on the sheared flow and groups of structures. Section 2 provides details of the numerical model and parametric studies. Section 3 presents two sets of obtained results. Section 4 summarizes the research findings.

2. Numerical Model

Sheared flow simulations in this work are performed for a system of three identical circular or D-shaped structures of the diameter d = 0.3 m. This set of structures is considered placed in proximity to a squared cylinder with a side equal to D = 5d in a rectangular fluid domain. CFD simulations are performed for the computational domain with a size of 30D × 16D, and the distance from the squared cylinder to the domain border is G = 20d. The incoming flow is entering the domain from the inlet left boundary, as illustrated in Figure 1a. The right boundary is considered to be the outlet, and the periodic and shadow boundary conditions are applied as the top and bottom boundaries.

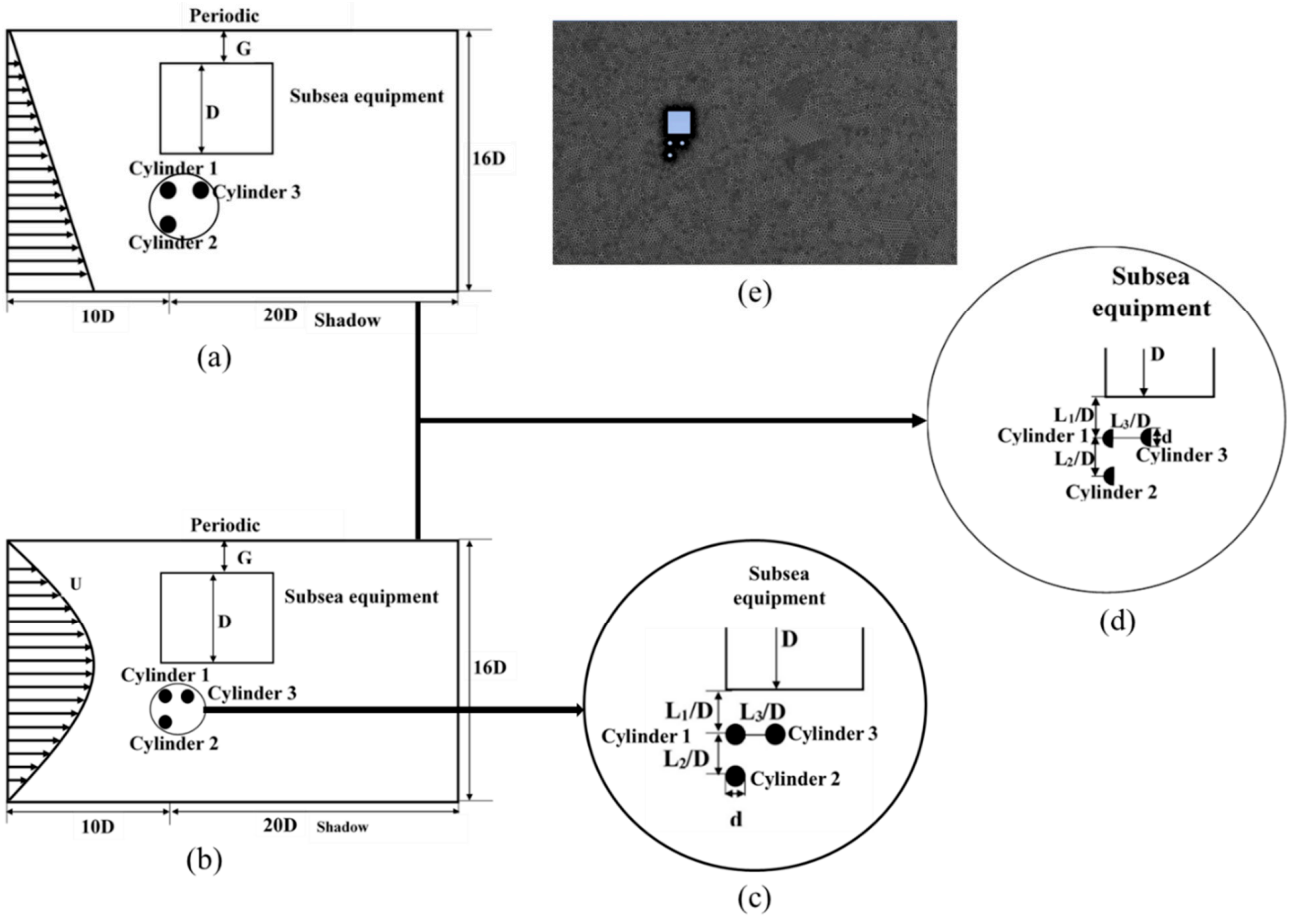

Figure 1. Rectangular computational fluid domain: (**a**) general schematic of the domain with four structures under the linearly sheared flow; (**b**) general schematic of the domain with four structures under the parabolic sheared flow; (**c**) enlarged group of smaller circular cylinders with the varying distances in between the structures defined; (**d**) arrangement with a group of smaller D-shaped cylinders with varying distances in between the structures subjected to both linear and parabolic sheared flow; (**e**) example of the mesh of the computational domain.

The parametric studies are performed for the spacing ratios L/D, with respect to the squared cylinder size of D, in the bandwidth from 0.6 to 1.0. Here, the variation of the L/D ratio is equivalent to the ratio L/d varying from 3.0 to 5.0, with respect to the circular cylinder size of d. Parametric investigations are organized in three different series. First, the L1, L2 and L3 distances between smaller structures are simultaneously varied from 0.6D to 1.0D while the structures are subjected to the linearly sheared flow. Second, the L1 size is kept constant at 0.6D, while distances L2 and L3 between smaller structures vary simultaneously from 0.6D to 1.0D and are subjected to both linear and parabolic sheared flows. Third, L1, L2 and L3 are kept constant at 0.6D between the D-shaped structures in both linear and parabolic sheared flows. Distance variations and corresponding case (arrangement) numbers are given in Table 1, where Case 1 is the base case, Cases 1–5 form the first series, Cases 1, 6–9 form the second series and the third series is consistent with distances in Case 1.

Table 1. Parametric investigations for the variation of distances between the structures.

Case Number	L_1/D	L_2/D	L_3/D
Case 1	0.6	0.6	0.6
Case 2	0.7	0.7	0.7
Case 3	0.8	0.8	0.8
Case 4	0.9	0.9	0.9
Case 5	1.0	1.0	1.0
Case 6	0.6	0.7	0.7
Case 7	0.6	0.8	0.8
Case 8	0.6	0.9	0.9
Case 9	0.6	1.0	1.0

The planar linear and parabolic sheared flows in this work, following the previous research in this direction [30,31], are defined using velocity profiles U, depending on the velocity U_c, consistent with the Reynolds number of 3900 at the centreline of the computational domain. The definition of the linear velocity profile is as follows:

$$U(y) = U_c - By, \tag{1}$$

where y is the vertical coordinate along the inlet boundary, and the gradient of the profile is $B = 0.022\ \mathrm{c}^{-1}$.

The parabolic sheared flow velocity profile is as follows:

$$U(y) = U_c(1 - (\frac{2y}{h})^2), \tag{2}$$

where h is the length of the inlet boundary.

Simulations are performed using the incompressible Navier-Stokes equation, k-ω SST turbulence model, PISO algorithm and the time step of 0.1 s. The triangular grid is used for simulation purposes, as shown in Figure 1e. The RANS equations are as follows:

$$\frac{\partial u_i}{\partial x_i} = 0, \tag{3}$$

$$\frac{\partial u_i}{\partial t} + u_j \frac{\partial u_i}{\partial u_j} = f_i - \frac{1}{\rho}\frac{\partial p}{\partial x_i} + \nu \frac{\partial^2 u_i}{\partial x_i \partial x_j}, \tag{4}$$

where $u(x)$ is the fluid velocity, $u(x) = \overline{u}(x) + u_\prime(x,t)$, with $x = (x,y)$ being the position vector for the two-dimensional analysis, t being the simulation time, $\overline{u}(x)$ being the mean velocity value and $u'(x,t)$ being the fluctuating velocity component. In Equation (4), ρ is the fluid density, p stands for the fluid pressure, f_i is the vector of external forces and i, j indicate two components of the velocity vector.

The mesh independence test results are reported in Table 2 for the uniform flow of the Reynolds number of 3900, including the mean drag coefficient C_{D0} and the dimensionless wall distance y+. The Mesh 3 from Table 2 is shown in Figure 1e and is selected for all the calculations in the next section. Since the k–ω SST turbulence model demands a very high near wall grid resolution, the maximum element size is fixed to be less than 1×10^{-4}.

Table 2. Mesh independency test results.

Cases	C_{D0}	Number of Cells	y^+
Current study at Re = 3900			
Mesh 1	0.87	31,297	0.0133
Mesh 2	0.91	53,951	0.0132
Mesh 3	0.93	86,637	0.0131
Mesh 4	0.93	153,227	0.0131
Published data at Re = 3900			
Norberg (1987), Experiment [36]	0.98	-	-
Franke and Frank (2002), LES [37]	0.99	-	-
Wornom et al. (2011), VMS-LES [38]	0.99	-	-
Ma et al. (2000), DNS [39]	0.96	-	-

Results are reported in the next section for three series of parametric investigations compared to the base case in terms of the lift coefficient amplitude of C_L, the fluctuating drag coefficient $C_D{}^{fl}$ and the mean drag coefficient C_{D0}. The drag coefficient C_D acting on the cylinder is defined as a sum of the mean drag coefficient C_{D0} and the fluctuating drag coefficient $C_D{}^{fl}$:

$$C_D = C_{D0} + C_D^{fl} \tag{5}$$

3. Results and Discussion

3.1. Simultaneous Variation of L_1/D, L_2/D and L_3/D in the Linearly Sheared Flow

The results of the first series of simulations for Cases 1–5 are summarized in Figure 2. Cylinder 2 in Figure 2a experiences the highest mean drag coefficient among smaller structures, with the maximum of 0.71 in Case 1. The mean drag coefficient for all three circular cylinders generally fluctuates as L/D increases. The variation of the mean drag coefficient of cylinder 1 and 2 with respect to L/D is less prominent, while cylinder 3 is subject to significant changes in all three considered fluid force coefficients, with unstable trends.

The maximum amplitude of the lift coefficient and fluctuating drag coefficient is observed for cylinder 3 at L/D = 0.75, as shown in Figure 2b,c, with a relatively prominent variation with L/D. Figure 3a,b show the variation of frequencies of the fluctuating drag and lift coefficients signal with L/D, respectively, where the statistics is presented for each circular structure. A maximum frequency is indicated here to be 0.023 Hz for the fluctuating drag coefficient signal and 0.015 Hz for the lift coefficient signal for the considered L/D range for cylinders 2 and 1 respectively. In this figure, cylinders 2 and 3 appear to have a similar frequency variation trend. All cylinders here display a change in fluid coefficient frequency patterns between L/D = 0.7 and L/D = 0.8, with higher frequency fluctuations at $L/D \leq 0.8$.

Figure 4 shows the distribution of the pressure along the surface of cylinders 1, 2 and 3 at the various L/D. For cylinder 1 at L/D = 0.6, the magnitude of the pressure becomes zero at θ = 149° and θ = 172°, while it reaches its maximum positive value at θ = 161° and maximum negative values at θ = 86° and θ = 221°. Here, zero pressure stands for the pressure in the fluid away from structures, where the flow is perturbed. At L/D = 0.7, the magnitude of the pressure becomes zero at θ = 159° and θ = 175°, with the maximum positive value observed at θ = 163° and maximum negative values observed at θ = 85° and θ = 226°. At L/D = 0.8, the magnitude of the pressure becomes zero at θ = 149° and θ = 176°, and reaches its maximum positive value at θ = 164° and its maximum negative values at θ = 89° and θ = 226°. At L/D = 0.9, the magnitude of the pressure becomes zero at θ = 146° and θ = 164°, and it reaches the maximum positive value at θ = 156° and the maximum negative values at θ = 88° and θ = 228°. Finally, at L/D = 1, the magnitude of

the pressure becomes zero at θ = 146° and θ = 161°, with the maximum positive value indicated at θ = 154° and maximum negative values observed at θ = 92° and θ = 230°.

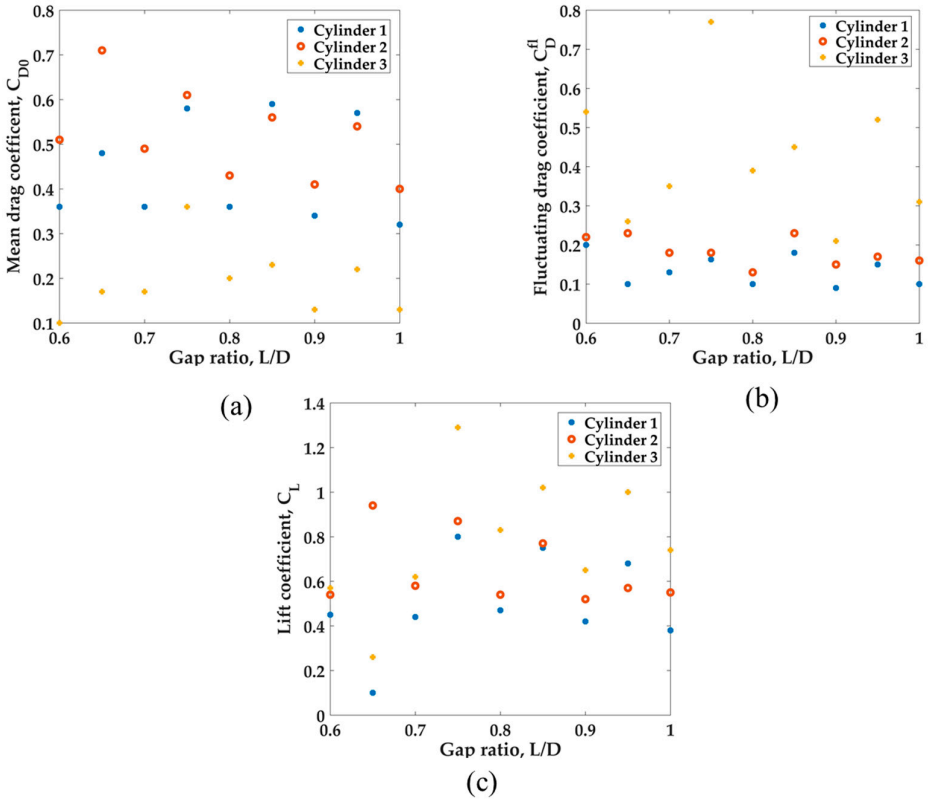

Figure 2. Trends in the fluid force coefficients with respect to the growth of the gap ratio L/D in the first set of simulations: (**a**) mean drag coefficient, (**b**) fluctuating drag coefficient, (**c**) lift coefficient.

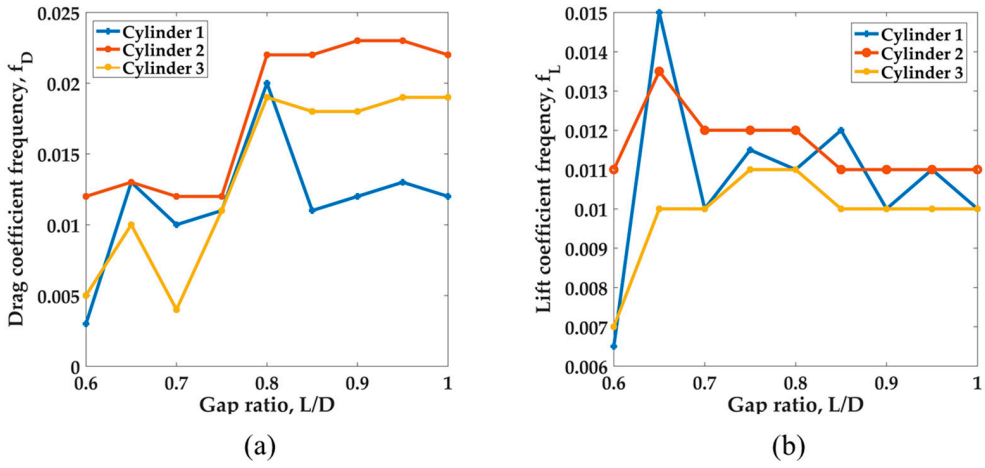

Figure 3. Trends in frequencies of the fluid force coefficients with respect to the growth of the gap ratio L/D in the first set of simulations: (**a**) for the fluctuating drag coefficient signal; (**b**) for the lift coefficient signal.

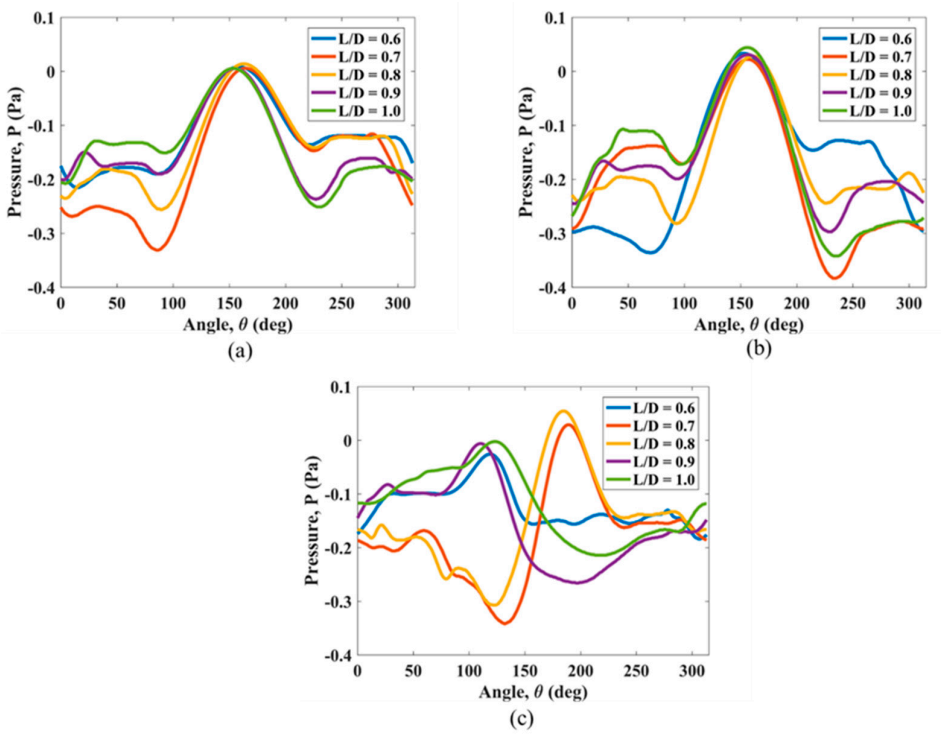

Figure 4. Pressure distribution along the surface of (**a**) cylinder 1, (**b**) cylinder 2, (**c**) cylinder 3, during the first series of simulations.

The time histories of hydrodynamic coefficients for three circular cylinders at different spacing ratios, varying simultaneously, are shown in Figures 5–7. In all figures, the gap ratio of L/D = 0.6 appears to have the most pronounced effect on the dynamics of both fluid forces. Both the fluctuating drag and lift coefficient time histories for all three structures display multi-frequency fluctuations at this spacing, although the dominant frequency of both signals, as shown in Figure 3, remains relatively close to the ones indicated by signals at other spacings. While the irregular nature of the lift coefficient at L/D = 0.6 manifests in additional fluctuations only, the fluctuating drag coefficient for all three structures displays overall higher amplitudes than for other considered gap ratios. The fluctuating drag amplitudes' jumps are observed to be the highest for cylinder 3, compared to other structures, as illustrated in Figure 7a. These changes are likely to be the consequence of the reattachment of shear layers, separated in the wake of cylinder 1. The fluctuating drag coefficient amplitudes for all spacings and for all circular cylinders also appear to be significantly asymmetric, compared to the nature of the lift coefficient signals for the cases considered.

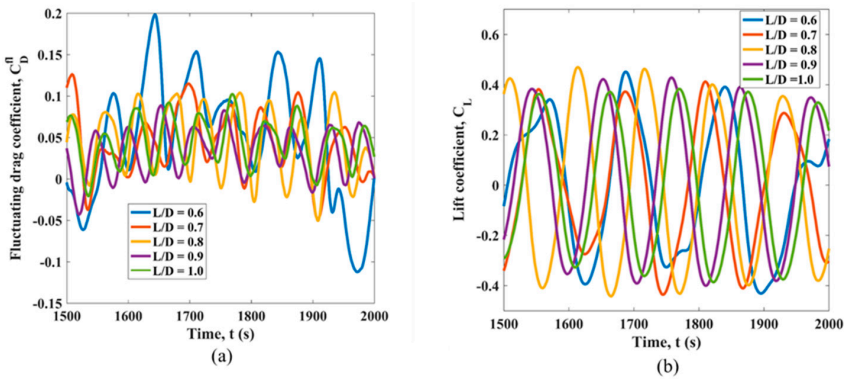

Figure 5. Fluid force coefficient time histories for cylinder 1 in the first set of simulations: (**a**) fluctuating drag coefficient; (**b**) lift coefficient.

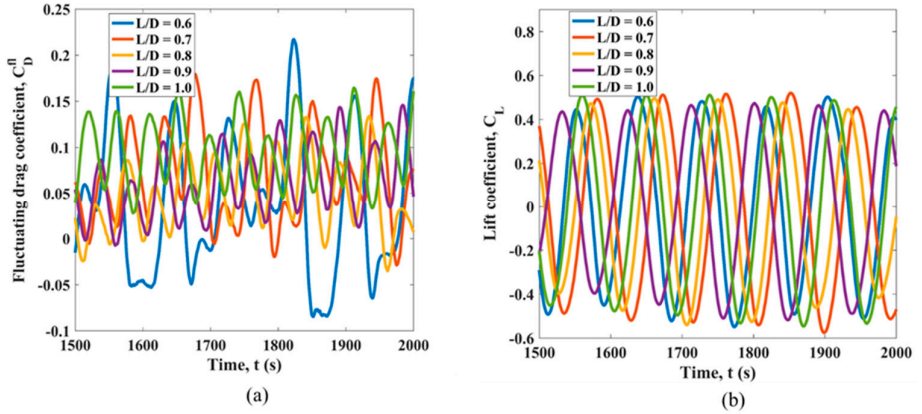

Figure 6. Fluid force coefficient time histories for cylinder 2 in the first set of simulations: (**a**) fluctuating drag coefficient; (**b**) lift coefficient.

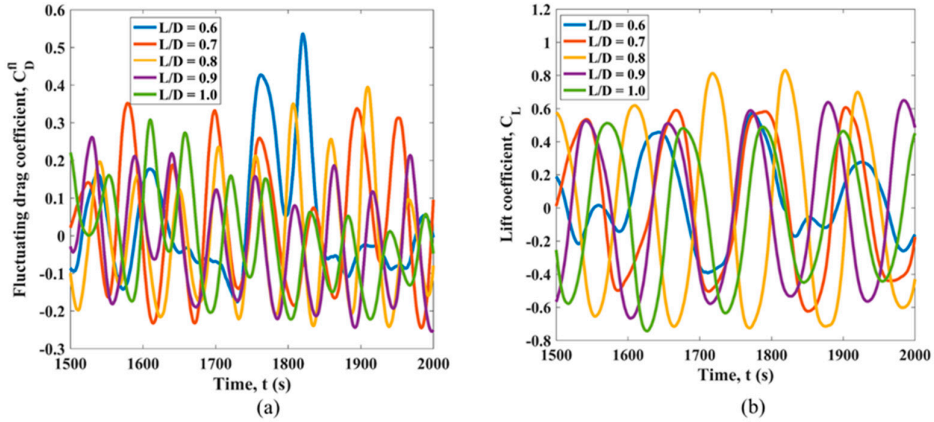

Figure 7. Fluid force coefficient time histories for cylinder 3 in the first set of simulations: (**a**) fluctuating drag coefficient; (**b**) lift coefficient.

3.2. Simultaneous Variation of L_2/D and L_3/D in the Linearly Sheared Flow

The second series of simulations starts with the consideration of the linear velocity profile. Changes to the mean drag coefficient value, maximum fluctuating drag coefficient and maximum amplitude of the lift coefficient for three smaller structures are shown in Table 3 for the constant gap ratio of L_1/D. The mean drag coefficient acting on cylinders 1 and 3 in Table 3 increases with the simultaneous growth of L_2/D and L_3/D. At the same time, the reduction in the mean drag coefficient is observed for cylinder 2 as it moves away from cylinder 1 and towards a high velocity region of the sheared flow profile, with a jump at L/D = 0.9. The variation of the fluctuating drag coefficient with L/D is prominent for cylinders 1 and 3 and is less pronounced for cylinder 2. The maximum value of the lift coefficient amplitude, according to Table 3, is largely affected for all structures, with the peak values observed at L/D = 0.8 or 0.9 and the strongest changes to forces acting on cylinder 3.

The statistics of the hydrodynamic coefficients' frequencies at a constant L_1/D is also summarized in Table 3. The frequency of the fluctuating drag coefficient signal for cylinder 1 increases with L/D. The maximum frequency of 0.023 Hz of the drag coefficient signal is observed for cylinder 2. At L/D = 0.8, the lift coefficient signals for cylinders 1 and 2 display the matching frequency. For cylinder 3, a gradual increase in the frequency of the lift coefficient is observed for L/D from 0.6 to 0.9, followed by a sharp decrease at L/D = 1.

Table 3. Result for simultaneous variation of L_2/D and L_3/D in the linearly sheared flow.

L/D	Cylinder 1					Cylinder 2					Cylinder 3				
	C_{D0}	C_D^{fl}	C_L	f_D	f_L	C_{D0}	C_D^{fl}	C_L	f_D	f_L	C_{D0}	C_D^{fl}	C_L	f_D	f_L
0.6	0.36	0.2	0.45	0.003	0.007	0.51	0.22	0.55	0.012	0.011	0.10	0.54	0.57	0.005	0.010
0.7	0.36	0.16	0.51	0.011	0.008	0.44	0.19	0.58	0.012	0.012	0.20	0.38	0.76	0.022	0.009
0.8	0.39	0.23	0.54	0.0125	0.012	0.41	0.20	0.58	0.014	0.012	0.16	0.46	0.78	0.023	0.010
0.9	0.40	0.20	0.49	0.013	0.010	0.45	0.19	0.54	0.012	0.010	0.19	0.46	0.88	0.021	0.012
1.0	0.40	0.13	0.45	0.014	0.011	0.43	0.17	0.49	0.023	0.011	0.18	0.32	0.79	0.021	0.010

Figure 8 demonstrates the velocity contour for L/D = 0.8 at the time of 2000 s in the simulation, when the flow is fully developed. In this setting, the vortices formed behind the squared cylinder have a strong influence on the vortices shed by the group of circular cylinders. The superposition of vortices first takes place behind cylinders 1 and 2 and then behind cylinder 3, where all occasional vortex pairs merge into a general 2S vortex street following this group for structures, which is relatively consistent in phase with the vortex formation behind the squared cylinder. The high fluctuating drag and lift coefficient amplitudes in Table 3 are closely related to this process. The half-cycle vortex shed by the larger structure towards the group of three smaller structures merges with their vortex street straightway into a grouped vortex formation. The vortex from another half-cycle behind the larger object becomes a separate vortex, as well as a single vortex separating from cylinder 2.

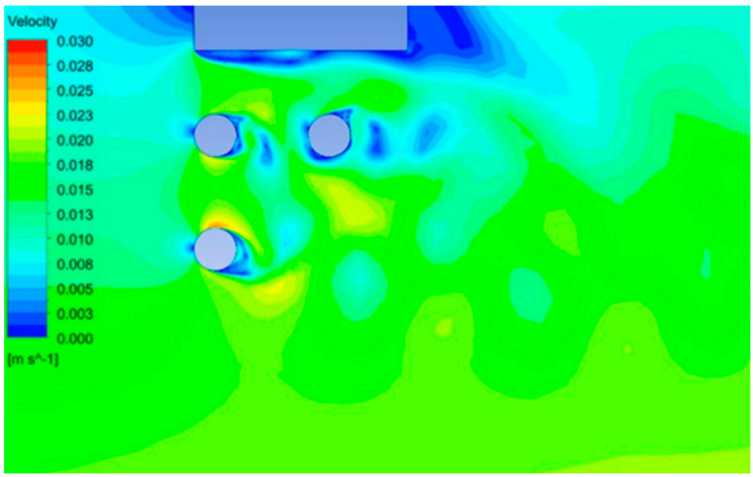

Figure 8. Velocity contour in the second set of simulations for L/D = 0.8 at 2000 s in the linearly sheared flow.

3.3. Simultaneous Variation of L_2/D and L_3/D in the Parabolic Sheared Flow

The second series of simulations is continued by considering the same structures in the parabolic flow. Table 4 shows the results of the hydrodynamic coefficients of three circular cylinders under the parabolic sheared flow, when the L_2/D and L_3/D ratios are simultaneously varied from 0.6 to 1.0. Here, upstream cylinders overall experience a higher mean drag coefficient and significantly higher lift coefficient amplitudes, as compared to the subsections above. This is due to their direct exposure to the sheared incoming flow. The variation of L/D has a significant effect on the hydrodynamic coefficients acting on structures. Cylinder 1 experiences a progressive increase in the mean drag coefficient from L/D = 0.6 to L/D = 0.9. A similar trend is observed for the linearly sheared flow in Table 3. However, the mean drag coefficient values in Table 4 for the parabolic flow are much higher compared to the data for the linearly sheared flow in Table 3. A similar observation is made

in the work [30]. The parabolic sheared flow leads to higher mean drag coefficient values for cylinder 2 than for cylinders 1 and 3 with the maximum value of 1.02 at L/D = 0.7. As observed for cylinder 1, cylinder 3 also experiences a progressive increase in the mean drag coefficient values with the maximum value of 0.38 at L/D = 0.9. Cylinders 1 and 3 have a higher fluctuating drag coefficient at L/D = 0.8 and 0.9 with cylinder 2 at L/D = 0.6 and 0.7. A maximum amplitude value of 1.92 of the lift coefficient is experienced by cylinder 2.

Table 4. Results for the parabolic sheared flow for circular cylinders.

L/D	Cylinder 1			Cylinder 2			Cylinder 3		
	C_{D0}	C_D^{fl}	C_L	C_{D0}	C_D^{fl}	C_L	C_{D0}	C_D^{fl}	C_L
0.6	0.68	0.29	0.62	1.01	0.84	1.72	0.14	0.27	0.58
0.7	0.75	0.29	0.63	1.02	0.84	1.91	0.29	0.40	1.30
0.8	0.94	0.70	1.52	0.87	0.65	1.66	0.34	0.70	1.34
0.9	1.0	0.87	1.65	0.95	0.67	1.74	0.38	0.80	1.57
1.0	0.93	0.67	1.43	0.88	0.60	1.41	0.37	0.56	1.23

The time histories of hydrodynamic coefficients and the corresponding FFT data for three circular structures under the parabolic sheared flow are displayed in Figures 9–11. A smaller amplitude of the fluctuating drag and lift coefficients is found for cylinder 1 at L/D = 0.6 and 0.7. The fluctuating drag and lift coefficient signals appear to be stable for the parabolic sheared flow, which is different from the linearly sheared flow, where signals seem to be unstable. The fluctuating drag coefficient of all three circular structures appears to be asymmetric towards the positive direction. A single dominating peak of the drag and lift coefficients is observed for cylinder 1, while multiple dominating peaks are observed for cylinders 2 and 3. Overall, the hydrodynamic forces in these cases show low frequency fluctuations.

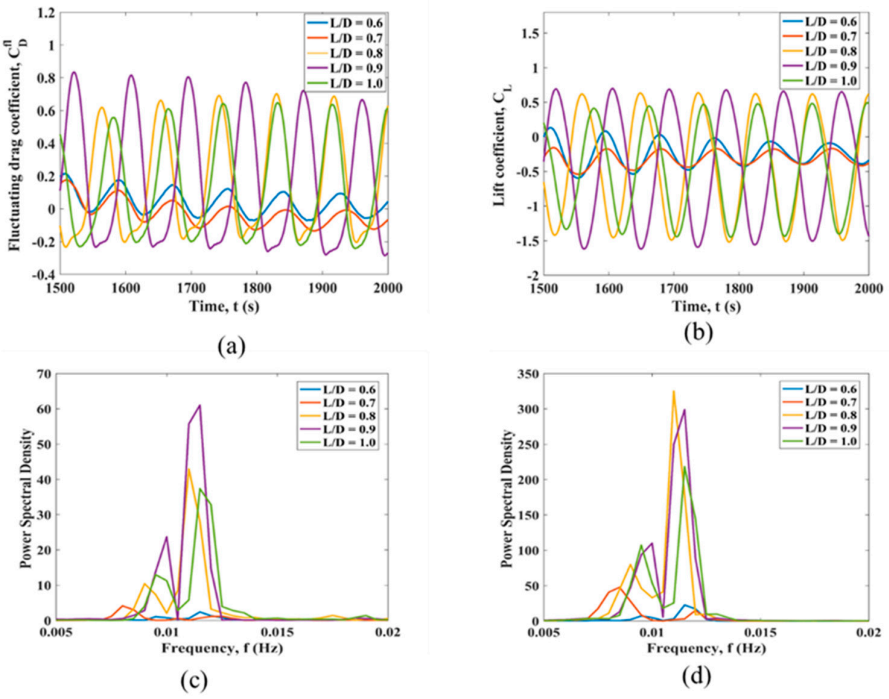

Figure 9. Fluid force coefficients for cylinder 1 immersed in the parabolic sheared flow in the second set of simulations: (**a**) time history of the fluctuating drag coefficient; (**b**) time history of the lift coefficient; (**c**) the fluctuating drag coefficient FFT; (**d**) the lift coefficient FFT.

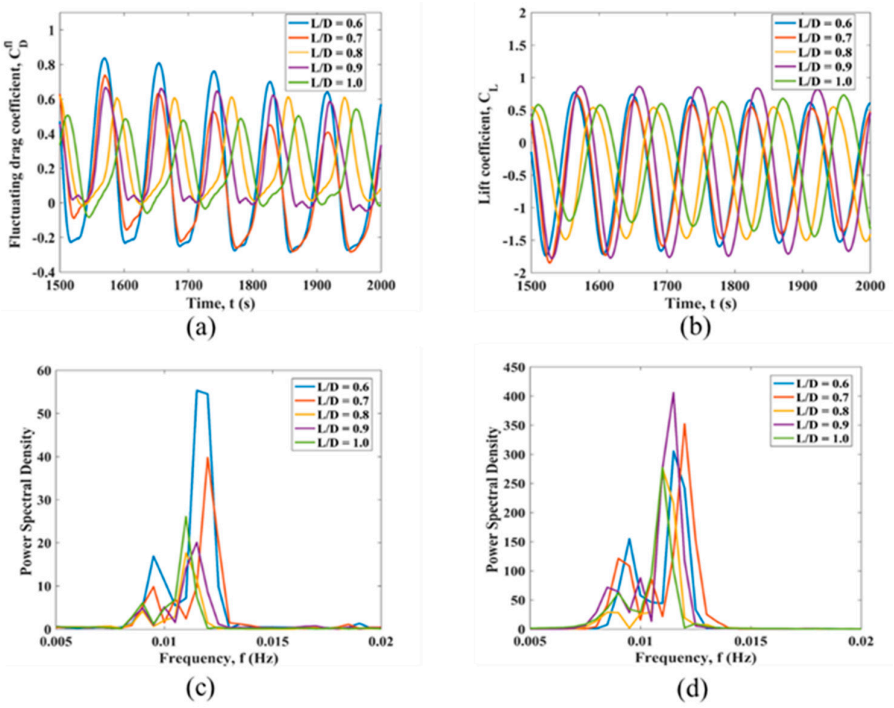

Figure 10. Fluid force coefficients for cylinder 2 immersed in the parabolic sheared flow in the second set of simulations: (**a**) time history of the fluctuating drag coefficient; (**b**) time history of the lift coefficient; (**c**) the fluctuating drag coefficient FFT; (**d**) the lift coefficient FFT.

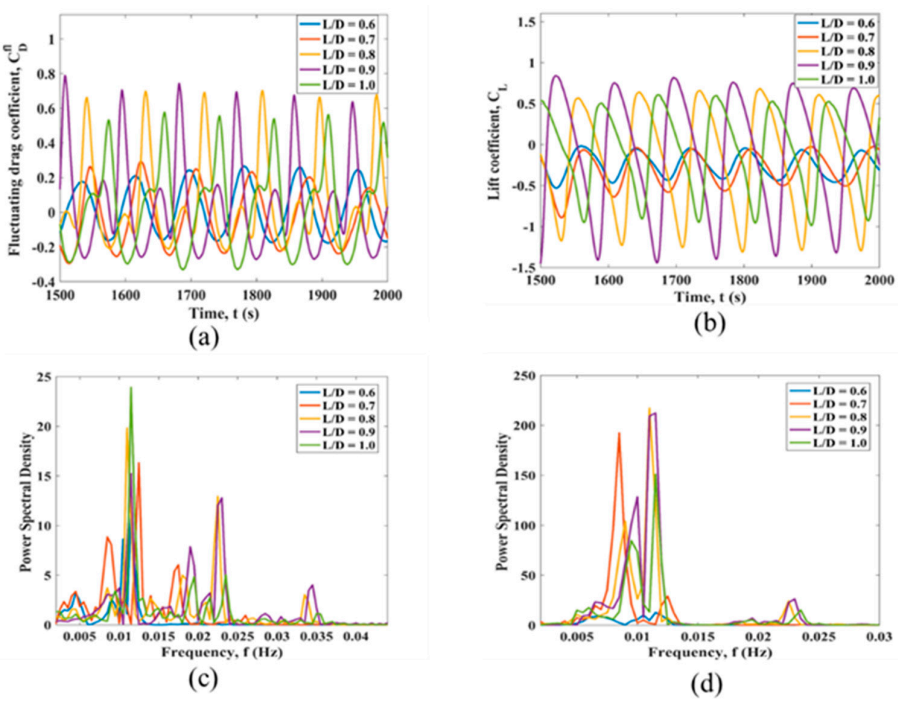

Figure 11. Fluid force coefficients for cylinder 3 immersed in the parabolic sheared flow in the second set of simulations: (**a**) time history of the fluctuating drag coefficient; (**b**) time history of the lift coefficient; (**c**) the fluctuating drag coefficient FFT; (**d**) the lift coefficient FFT.

Figure 12 shows the velocity contour for L/D = 0.8 at the time of 2000 s in the simulation in the parabolic sheared flow, when the flow is fully developed. In this case, the vortices formed behind the squared cylinder have a strong influence on the vortices shed by the group of circular cylinders, especially by circular cylinder 3. The superposition of

vortices first takes place behind cylinders 1 and 2 and then behind cylinder 3. This process is similar to the linearly sheared flow, where the vortices in the center of domain form a vortex group behind the structures, while the final vortex street is dominated by the phase of the vortex formation behind the squared cylinder.

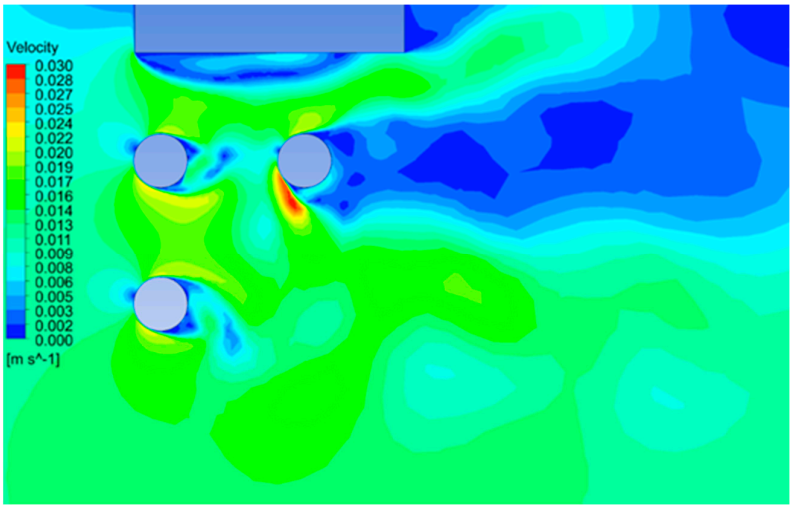

Figure 12. Velocity contour in the second set of simulations for L/D = 0.8 at 1000 s in the parabolic sheared flow.

3.4. Simulations for D-Shaped Structures in Linear and Parabolic Sheared Flow

The third simulation series considers smaller structures of a D-shaped cross-section. Table 5 shows the hydrodynamic coefficients of three D-shaped cylinders under the linear and parabolic sheared flow at a constant L/D = 0.6. Both flow profiles result in an increase in the mean drag coefficient of upstream cylinders. The mean drag values and maximum fluctuating drag and lift coefficient amplitudes are generally higher for the parabolic sheared flow profile. The D-shaped cylinder 2, under both flow profiles, experiences the highest hydrodynamic loads.

Table 5. Hydrodynamic coefficients for D-shaped cylinders in two sheared flows and at a constant spacing.

Constant L/D	Cylinder 1			Cylinder 2			Cylinder 3		
	C_{D0}	C_D^{fl}	C_L	C_{D0}	C_D^{fl}	C_L	C_{D0}	C_D^{fl}	C_L
Linearly sheared flow									
0.6	0.63	0.32	0.51	0.92	0.50	0.80	0.10	0.25	0.46
Parabolic sheared flow									
0.6	1.01	0.79	1.03	1.43	1.08	1.42	0.25	0.85	1.03

D-shaped cross-sections are considered in the literature [33,34] as overall reducing the drag force. However, at L/D = 0.6 in the present work, as shown in Table 5, the D-shaped cylinders indicate a higher mean drag coefficient, with relatively lower values in the case of a linearly sheared current. The time histories of the fluctuating drag and lift coefficients for both flow profiles are compared for three structures in Figure 13. Here, the fluctuations in the hydrodynamic loads on cylinder 2 in the parabolic flow are substantially asymmetric, which appears to be a combined effect of the proximity to a larger object, flow velocity profile and type of the cross-section. Figure 14 illustrates velocity contours for both linear and parabolic sheared flows at the simulation time of 2000 s, which indicates several regions of the vortex formation, as considered in detail in the following subsection.

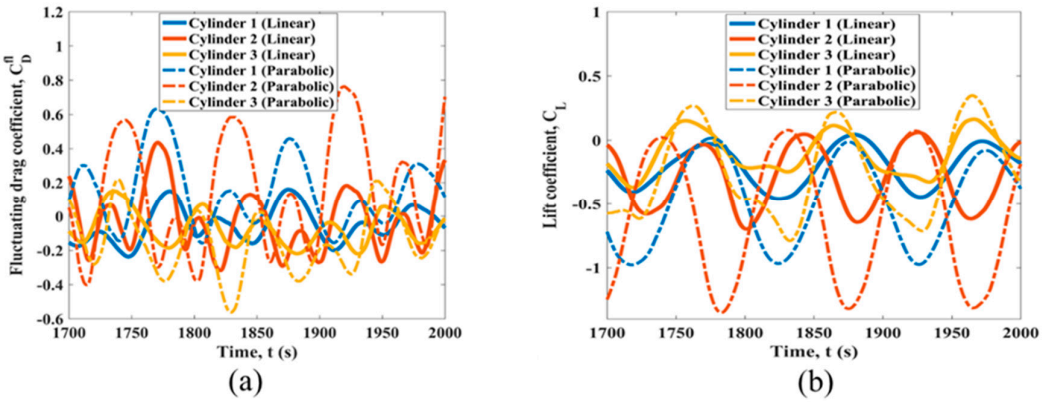

Figure 13. Fluid force coefficients for three D-shaped cylinders immersed in the linear and parabolic sheared flow in the third set of simulations: (**a**) time history of the fluctuating drag coefficient; (**b**) time history of the lift coefficient.

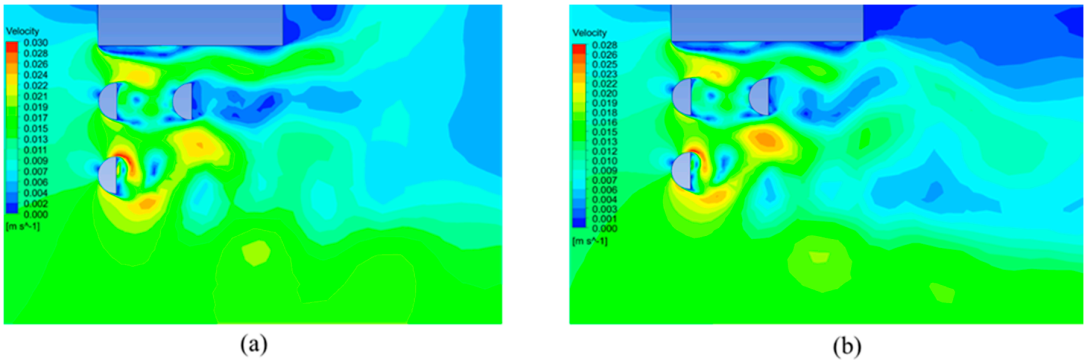

Figure 14. Velocity contour in the third set of simulations for L/D = 0.6 at 2000 s: (**a**) in the parabolic sheared flow profile, (**b**) in the linearly sheared flow.

The formation of individual vortex streets behind D-shaped structures and a larger cylinder with the following merging into a single Karman street is shown for the parabolic turbulent flow in Figure 15 in the form of streamlines. Here, the simulation times of 1000 s and 2000 s show two different phases of the vortex shedding cycle. The vorticity variable in Figure 16 demonstrates a minor vortex to be excited from the surface of cylinder 2. Vortex streets from cylinders 1 and 3 merge and alter the vortex formation cycle from the larger structure, with greater fluctuations in the flow on the side of smaller structures. Here, the 2S vortex street from the squared cylinder transforms into a combination of about six vortices formed per cycle, with a group of four vortices in the center of the street, as indicated in Figure 17.

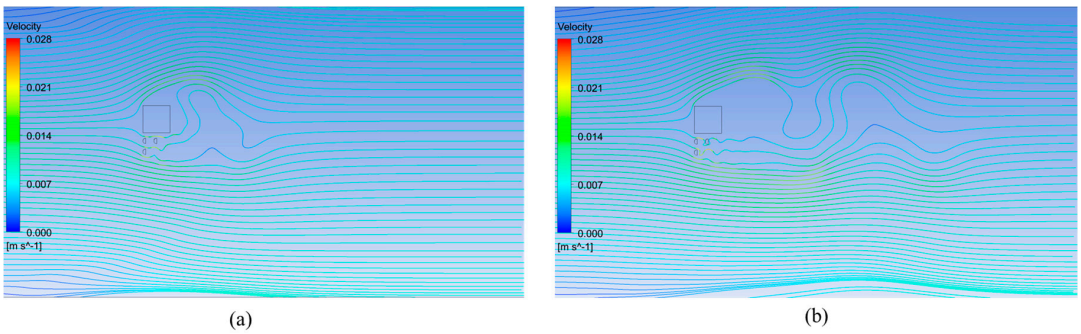

Figure 15. Streamlines for the D-shaped cylinders in the parabolic sheared flow at the simulation time of: (**a**) 1000 s and (**b**) 2000 s.

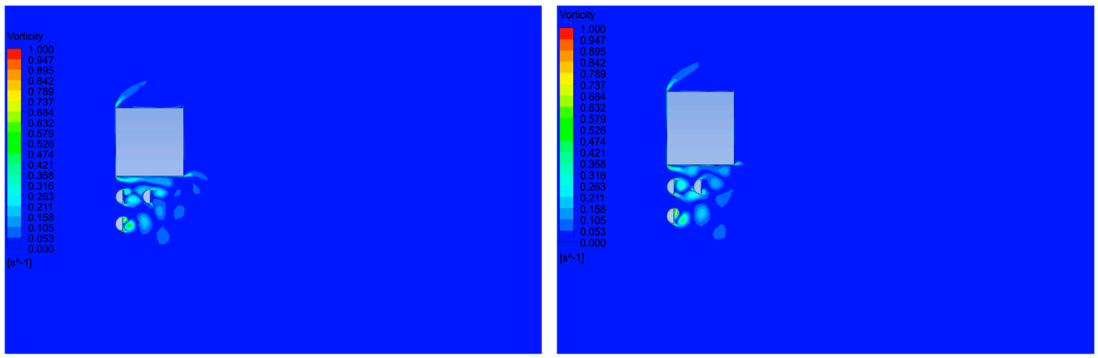

Figure 16. Vorticity contour for the D-shaped cylinders in the parabolic sheared flow at the simulation time of: (**a**) 1000 s and (**b**) 2000 s.

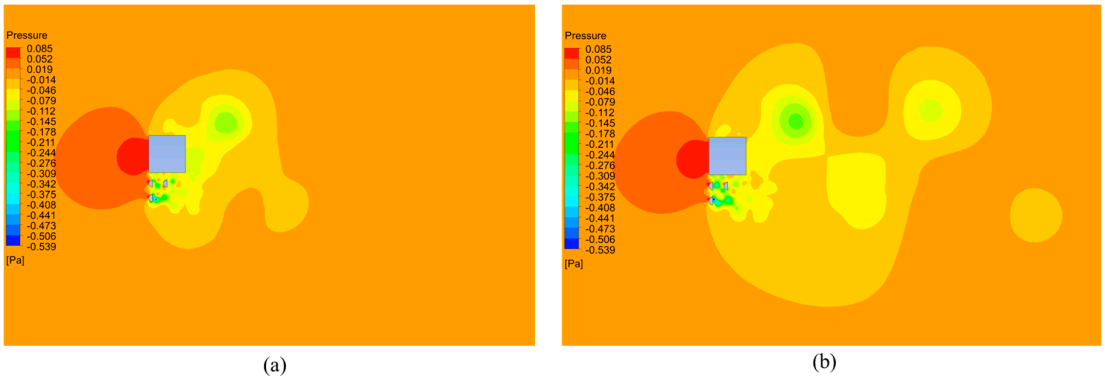

Figure 17. Pressure contour for the D-shaped cylinders in the parabolic sheared flow at the simulation time of: (**a**) 1000 s and (**b**) 2000 s.

4. Conclusions

This study presents a comprehensive numerical investigation on the flow over three identical circular and D-shaped cylinders in close proximity to subsea equipment modeled as a squared cylinder. The 2D linear and parabolic sheared flow velocity profiles based on the Reynolds number of 3900 are analyzed, and simulations are performed using the k–ω SST turbulence model.

Three series of parametric investigations reveal notable changes to the mean drag coefficient on cylinder 1 and the fluctuating drag coefficient acting on cylinder 3.

Keeping the L_1/D constant, during the second simulation series, leads to an increase in the mean drag coefficient of upstream cylinders with the growth of the gap ratio for both flow profiles. The parabolic sheared flow profile in this series produces the highest mean drag, fluctuating drag and maximum amplitude of the lift coefficient signal. The fluctuations of the drag and lift coefficients appear more stable in the parabolic flow than in the linear flow.

Changing the geometrical shape of circular cylinders to a D-shape and assuming a constant $L/D = 0.6$ between the structures results in an increase in the hydrodynamic coefficient values for both sheared flow profiles. The parabolic profile is found to lead to higher hydrodynamic coefficients than observed for the linearly sheared current. In this arrangement, D-shaped structures do not display an advantageous reduction in hydrodynamic loads, as was found in previous studies.

All vortex streets observed for simulated sheared flow profiles appear to be complex. Vortex streets in the wake from the group of smaller cylinders in the cases considered appear to combine into a single vortex street, while a separate Karman street with larger vortices forms in the wake of the squared structure. These two vortex streets merge on one

side and form a vortex group, and this interaction defines increased hydrodynamic loads in the considered sheared flow. Future work in this direction may consider a wider range of Reynolds numbers as a part of sheared flow variations and changes to the relative sizes of structures.

Author Contributions: Conceptualization, methodology, H.F.A. and V.K.; software, validation, investigation, data curation, writing—original draft preparation, H.F.A.; writing—review and editing, supervision, project administration, funding acquisition, V.K. All authors have read and agreed to the published version of the manuscript.

Funding: The authors would like to acknowledge the support of the National Project "Science and Universities" of the Ministry of Science and Higher Education of the Russian Federation, grant number FEWN-2021-0012.

Institutional Review Board Statement: Not applicable.

Informed Consent Statement: Not applicable.

Data Availability Statement: Data can be available upon a reasonable request to the e-mail of the corresponding author.

Conflicts of Interest: The authors declare no conflict of interest.

References

1. Jordan, S.K.; Fromm, J.E. Laminar flow past a circle in shear flow. *Phys. Fluids* **1972**, *15*, 972–976. [CrossRef]
2. Williamson, C.H.K. Vortex dynamics in the cylinder wake. *Annu. Rev. Fluid Mech.* **1996**, *28*, 477–539. [CrossRef]
3. Zdravkovich, M.M. Review of flow interference between two circular cylinders in various arrangements. *ASME J. Fluids Eng.* **1977**, *99*, 618–633. [CrossRef]
4. Breuer, M. A challenging test case for large eddy simulation: High Reynolds number circular cylinder flow. *Int. J. Heat Fluid Flow* **2000**, *21*, 648–654. [CrossRef]
5. Lei, C.; Cheng, L.; Kavanagh, K. Spanwise length effects on three-dimensional modelling of flow over a circular cylinder. *Comput. Method Appl. Mech.* **2001**, *190*, 2909–2923. [CrossRef]
6. Labbé, D.F.L.; Wilson, P.A. A numerical investigation of the effects of the spanwise length on the 3-d wake of a circular cylinder. *J. Fluids Struct.* **2007**, *23*, 1168–1188. [CrossRef]
7. Xu, W.; Haokai, W.; Kun, J.; Enhao, W. Numerical investigation into the effect of spacing on the flow-induced vibrations of two tandem circular cylinders at subcritical Reynolds numbers. *Ocean Eng.* **2021**, *236*, 1–19. [CrossRef]
8. Yoshino, F.; Hayashi, T. Numerical solution of flow around a rotating circular cylinder in uniform shear flow. *Bull. JSME* **1984**, *27*, 1850–1857. [CrossRef]
9. Tamura, H.; Kiya, M.; Arie, M. Numerical study on viscous shear flow past a circular cylinder. *Bull. JSME* **1989**, *23*, 1952–1958. [CrossRef]
10. Ayukawa, K.; Ochi, J.; Kawahara, G.; Hirao, T. Effects of shear rate on the flow around a square cylinder in a uniform shear flow. *J. Wind. Eng. Ind. Aerodyn.* **1993**, *50*, 97–106. [CrossRef]
11. Lei, C.; Cheng, L.; Kavanagh, K. A finite difference solution of the shear flow over a circular cylinder. *Ocean Eng.* **2000**, *27*, 271–290. [CrossRef]
12. Wu, T.; Chen, C.-F. Laminar boundary-layer separation over a circular cylinder in uniform shear flow. *Acta Mech.* **2000**, *144*, 71–82. [CrossRef]
13. Sumner, D.; Akosile, O.O. On uniform planar shear flow around a circular cylinder at subcritical Reynolds number. *J. Fluids Struct.* **2003**, *18*, 441–454. [CrossRef]
14. Kang, S. Uniform-shear flow over a circular cylinder at low Reynolds numbers. *J. Fluids Struct.* **2006**, *22*, 541–555. [CrossRef]
15. Shuyang, C.; Shigehira, O.; Yukio, T.; Yaojun, G.; Hironori, K. Numerical simulation of Reynolds number effects on velocity shear flow around a circular cylinder. *J. Fluids Struct.* **2010**, *26*, 685–702.
16. Gao, Y.; Zhang, Y.; Zhao, M.; Wang, L. Numerical investigation on two degree-of-freedom flow-induced vibration of three tandem cylinders. *Ocean Eng.* **2020**, *201*, 107059. [CrossRef]
17. Zhao, M.; Cheng, L. Numerical simulation of vortex-induced vibration of four circular cylinders in a square configuration. *J. Fluids Struct.* **2012**, *31*, 125–140. [CrossRef]
18. Han, Z.; Zhou, D.; He, T.; Tu, J.; Li, C.; Kwok, K.C.; Fang, C. Flow-induced vibrations of four circular cylinders with square arrangement at low Reynolds numbers. *Ocean Eng.* **2015**, *96*, 21–33. [CrossRef]
19. Gao, Y.; Yang, K.; Zhang, B.; Cheng, K.; Chen, X. Numerical investigation on vortex-induced vibrations of four circular cylinders in a square configuration. *Ocean Eng.* **2019**, *175*, 223–240. [CrossRef]
20. Gómez, H.A.; Narváez, G.F.; Schettini, E.B. Vortex induced vibration of four cylinders configurations at critical spacing in 0° and 45° flow incidence angle. *Ocean Eng.* **2022**, *252*, 111134. [CrossRef]

21. Xu, W.; Zhang, S.; Liu, B.; Wang, E.; Bai, Y. An experimental study on flow-induced vibration of three and four side-by-side long flexible cylinders. *Ocean Eng.* **2018**, *169*, 492–510. [CrossRef]
22. Wang, E.; Xu, W.; Yu, Y.; Zhou, L.; Incecik, A. Flow-induced vibrations of three and four long flexible cylinders in tandem arrangement: An experimental study. *Ocean Eng.* **2019**, *178*, 170–184. [CrossRef]
23. Han, P.; Pan, G.; Zhang, B.; Wang, W.; Tian, W. Three-cylinder oscillator under flow: Flow induced vibration and energy harvesting. *Ocean Eng.* **2020**, *211*, 107619. [CrossRef]
24. Xu, W.; Zhang, S.; Ma, Y.; Liu, B. Fluid forces acting on three and four long side-by-side flexible cylinders undergoing flow-induced vibration (FIV). *Mar. Struct.* **2021**, *75*, 102877. [CrossRef]
25. Fan, X.; Wang, Z.; Wang, Y.; Tan, W. The effect of vortices structures on the flow-induced vibration of three flexible tandem cylinders. *Int. J. Mech. Sci.* **2021**, *192*, 106132. [CrossRef]
26. Ma, Y.; Xu, W.; Liu, B. Dynamic response of three long flexible cylinders subjected to flow-induced vibration (FIV) in an equilateral-triangular configuration. *Ocean Eng.* **2019**, *183*, 187–207. [CrossRef]
27. Liu, Y.; Li, P.; Wang, Y.; Chen, X.; Ren, X.; Lou, M. Dynamic response of five-riser group subjected to vortex-induced vibration in a cylindrical arrangement configuration. *Ocean Eng.* **2022**, *254*, 111271. [CrossRef]
28. Silva-Ortega, M.; Assi, G.R.S. Flow-induced vibration of a circular cylinder surrounded by two, four and eight wake-control cylinders. *Exp. Therm. Fluid Sci.* **2017**, *85*, 354–362. [CrossRef]
29. de Oliveira Barbosa, J.M.; Qu, Y.; Metrikine, A.V.; Lourens, E.M. Vortex-induced vibrations of a freely vibrating cylinder near a plane boundary: Experimental investigation and theoretical modelling. *J. Fluids Struct.* **2017**, *69*, 382–401. [CrossRef]
30. Annapeh, H.F.; Kurushina, V. Effect of Gap and Diameter Ratio on Vortex-Induced Forces for Cylinders in Tandem at Re = 100. In *Journal of Physics: Conference Series*; IOP Publishing: Bristol, UK, 2022; Volume 2219, p. 012021.
31. Annapeh, H.F.; Kurushina, V. Numerical Simulation of Flow-Induced Forces on Subsea Structures in a Group under Uniform and Sheared Flow. In *International Conference on Wave Mechanics and Vibrations*; Springer: Cham, Switzerland, 2023; pp. 512–522.
32. Annapeh, H.F.; Kurushina, V. Analysis of vortex-induced forces on the group of subsea structures in proximity of equipment at Re = 3900. *J. Math. Struct. Model.* **2022**, *4*, 60–74.
33. Annapeh, H.F.; Kurushina, V. Hydrodynamic Loads on a Group of Six Structures of Different Cross-Sections in Uniform and Sheared Flow. *J. Mar. Sci. Eng.* **2023**, *11*, 383. [CrossRef]
34. Zhao, J.; Thompson, M.C.; Hourigan, K. Flow-Induced Vibration of a D-Shape Cylinder. In Proceedings of the European Nonlinear Dynamics Conference, Budapest, Hungary, 25–30 June 2017.
35. Postnikov, A.; Pavlovskaia, E.; Wiercigroch, M. 2DOF CFD calibrated wake oscillator model to investigate vortex-induced vibrations. *Int. J. Mech. Sci.* **2017**, *127*, 176–190. [CrossRef]
36. Norberg, C. *Effects of Reynolds Number and Low-Intensity Free-Stream Turbulence on the Flow around a Circular Cylinder*; Publ. No. 87/2; Department of Applied Thermoscience and Fluid Mechanics, Chalmers University of Technology: Göteborg, Sweden, 1987.
37. Franke, J.; Frank, W. Large eddy simulation of the flow past a circular cylinder at ReD = 3900. *J. Wind. Eng. Ind. Aerodyn.* **2002**, *90*, 1191–1206. [CrossRef]
38. Wornom, S.; Ouvrard, H.; Salvetti, M.V.; Koobus, B.; Dervieux, A. Variational multiscale large-eddy simulations of the flow past a circular cylinder: Reynolds number effects. *Comput. Fluids* **2011**, *47*, 44–50. [CrossRef]
39. Ma, X.; Karamanos, G.-S.; Karniadakis, G.E. Dynamics and low-dimensionality of a turbulent near wake. *J. Fluid Mech.* **2000**, *410*, 29–65. [CrossRef]